



<http://www.diva-portal.org>

Postprint

This is the accepted version of a paper published in *Journal of Computational Physics*. This paper has been peer-reviewed but does not include the final publisher proof-corrections or journal pagination.

Citation for the original published paper (version of record):

Ahmad, M., Islam, S-u., Larsson, E. (2020)

Local meshless methods for second order elliptic interface problems with sharp corners

Journal of Computational Physics, 416: 109500

<https://doi.org/10.1016/j.jcp.2020.109500>

Access to the published version may require subscription.

N.B. When citing this work, cite the original published paper.

Permanent link to this version:

<http://urn.kb.se/resolve?urn=urn:nbn:se:uu:diva-414049>

Local meshless methods for second order elliptic interface problems with sharp corners

Masood Ahmad¹

Siraj-ul-Islam^{1*}

Elisabeth Larsson²

¹Department of Basic Sciences, University of Engineering and Technology, Peshawar, Pakistan.

² Scientific Computing, Department of Information Technology, Uppsala University, Sweden.

May 17, 2020

Abstract

In the present paper, we develop a local meshless procedure for solving a steady state two-dimensional interface problem having discontinuous coefficients and curved interfaces with sharp corners. The proposed local meshless methods are based on three types of radial basis functions (RBFs): a local meshless method based on multiquadric RBF (LMM1P), a local meshless method based on integrated multiquadric RBF (LMM2P) and a local meshless method based on hybrid Gaussian-Cubic RBF (LMM3P). Stencils are designed at the interface and interior regions to cope with discontinuities and sharp corners. Due to the localized nature of the procedure and a sparse matrix representation, the local meshless methods become computationally less expensive than global meshless methods. The methods are augmented with linear polynomial to improve accuracy and ensure stable computation. Comparison with some existing versions of finite element methods is also performed to show better accuracy of the proposed meshless methods. Accuracies of the proposed local meshless methods are also compared among themselves. Flexibility of the meshless methods with respect to complex geometries, adapting to different shapes of the interfaces and selection of the shape parameter is also considered.

Keywords: Local meshless method, radial basis functions, elliptic interface model, sharp-edged interface, sparse matrix, collocation

1 Introduction

Purpose built accurate numerical methods for Poisson-Boltzmann type of PDEs with non-smooth interfaces or interfaces with Lipschitz continuity are required due non-availability of closed form solution. These PDEs are important from solution point of view due to their essential role in mathematical modelling of many physical situations. Such models contain geometric singularities in the form of cusps and self-intersecting surfaces, thus creating accuracy issues for many numerical methods. Geometric singularities lead to so-called solution singularities. In some situations, electric field is singular in the vicinity of geometric singularities as observed at tips of electrodes and at sharp edges of planar conductors [1]. Numerical solution of elliptic PDEs with

*The author to whom all the correspondence should be addressed. Email: siraj.islam@gmail.com (Siraj-ul-Islam), masood.suf@gmail.com (Masood Ahmad)

discontinuous coefficients, representing non-smooth interfaces, are challenging problems and their applications can be found in many areas of science and engineering [2], such as wave-guides analysis [3], plasma-surface interaction [4], turbulent-flow [5], friction modelling and electromagnetic wave scattering and propagation [6, 7].

In the present work, we consider a two-dimensional steady state interface problem, where the interfaces have sharp corners and the coefficients may be discontinuous. The model under consideration to be solved numerically is of the form

$$\nabla \cdot (\beta_1 \nabla v_1) + k_1 v_1 = f_1, \quad \text{in } \Omega_1, \quad (1a)$$

$$\nabla \cdot (\beta_2 \nabla v_2) + k_2 v_2 = f_2, \quad \text{in } \Omega_2, \quad (1b)$$

$$v_2 = h, \quad \text{on } \partial\Omega \setminus \Gamma, \quad (1c)$$

$$v_2 - v_1 = g_1, \quad \text{on } \Gamma, \quad (1d)$$

$$\beta_2 \nabla v_2 \cdot \mathbf{n}_2 - \beta_1 \nabla v_1 \cdot \mathbf{n}_1 = g_2, \quad \text{on } \Gamma, \quad (1e)$$

$$(1f)$$

where $v_1 = v_1(x, y)$ and $v_2 = v_2(x, y)$, $g_1 = g_1(x, y)$ and $g_2 = g_2(x, y)$, \mathbf{n}_1 and \mathbf{n}_2 are the outward normals of the domains Ω_1 and Ω_2 respectively, such that $\Omega = \Omega_1 \cup \Omega_2$ and $\Gamma = \Omega_1 \cap \Omega_2$. Such type of models has wide applications in fluid mechanics, material science, electromagnetic wave propagation and biological sciences [8]. The additional interface conditions (1d) and (1e) need to be enforced in order to accurately solve the given elliptic interface problem. Appropriate numerical treatment of the interface conditions is essential, otherwise, the errors would grow substantially, causing an invalid solution [9].

Some technical contributions towards the numerical solution of parabolic and elliptic PDEs related to diffusive transport processes in the interface embedded domains have been reported in [8, 10–19] and the references therein. Methodologies reported in these papers are the different variants of either FEM or FDM with a purpose built treatment for the interfaces during the design of the algorithm in the form of an interface fitted mesh, cut finite elements or immersed finite element methods. Despite huge successes offered by these methods and allied remedial measures, the classical numerical methods still encounter difficulties while dealing with discontinuities or sharp interface corners, due non-coincidence of the interfaces with the original computational mesh edges. Re-meshing procedures, which is one of the remedies, are costly and non-trivial for two- and three-dimensional PDEs.

As a matter of fact, the gradient is not well defined near the tips of sharp interface corners and some earlier interface methods might not work in this context [2]. Finite element methods can become costly memory-wise due to the requirement of local mesh refinement in the vicinity of sharp corners [20]. Also, local mesh refinement does not produce good accuracy when the solution is highly oscillatory as witnessed in electromagnetic wave scattering and propagation [21], vibration analysis of engineering structures, and shock-vortex interactions in compressible fluid flows. It is truly difficult to design high order converging interface schemes for arbitrarily complex interface geometries [1]. A finite element formulation reported in [22] was designed for solving elliptic PDEs with sharp-edged interfaces, while attaining about 0.8th order convergence on non-body fitted grids.

These challenges have motivated us to explore the rich dynamics of the meshless methods as an alternate numerical method in the context of PDEs with interface conditions. Recently, great attention has been paid to different types of (localized) meshless approximations used for numerical solution of PDEs and integral equations due to some inherent advantages. The prime distinction among these is the ability of meshless methods to adapt the stencils to approximate

local behaviour and tackle difficulties caused by the interface conditions. This can be achieved by the meshless methods without re-meshing coupled with flexibility with respect to the geometry and ease of extension to higher dimensions. Unlike the conventional methods, meshless methods can cope with scattered data and irregular geometries should the need arise. Meshless methods based on differential quadrature [23] (also known as RBF-FD methods) with global integrated RBFs and ordinary RBFs have recently been used in [24–27] for numerical solution of steady and unsteady interface PDEs in irregular domain settings (see also [28]).

In the construction of strong form meshless approximations, RBFs can be used both globally and locally. Localized meshless approximations using RBFs is preferred due to computational advantages such as almost banded/sparse matrix representation and less sensitivity to the shape parameter. Unlike the global meshless formulation, the stencil weights in the local meshless strong formulation are determined by inversion of small well-conditioned matrices, there is the involvement of a large differential quadrature matrix when the underlying PDE is elliptic type. Another benefit of the localized methods is the flexibility of the stencil selection and the nodal point selection to improve accuracy of the method. For instance, nodes can be used in the local support domain on the upwind side to obtain a physically viable solution in the case of some boundary layer problems and convection-dominated PDEs [23, 29–31].

Unlike the local meshless methods based on RBFs, the shape parameter deeply affects the accuracy of the global meshless RBF-based methods. Sensitivity of the local RBF methods to the shape parameter is comparatively lower than the sensitivity to the shape parameter of the global counterpart, and hence more caution is needed while employing global RBFs for numerical approximation of PDEs. Generally, we do not have both good accuracy and well-conditioning simultaneously in the RBF approximation methods [32]. This situation arises partly because of the lack of theoretical frameworks for adjusting the shape parameter value with respect to accuracy and stability of the numerical method while using shape parameter-dependent RBFs. Many researchers have proposed different algorithms for finding relatively optimal shape parameter values. For more details the reader is referred to [33–40] and the references therein. Alternatively, a stable evaluation method can be used, that eliminates sensitivity to the shape parameter [41–45]. Common for these stable methods is that the stability comes with an increase in computational cost.

It has been found in previously reported work that performance of integrated RBFs [24, 27, 33] is better than that of conventional RBFs in terms of accuracy, computational stability, and sensitivity to the shape parameter. Due to use of the integrated RBF-based meshless methods, an inherent disadvantage of ill-conditioning of the global meshless methods is minimized up to some extent, but cannot be eliminated completely due to the large size of the coefficient matrix.

Recently, a hybrid Gaussian-cubic RBF was proposed [46] to reduce the ill-conditioning problem in RBF approximation and obtain better convergence in the case of single phase PDEs. The basic idea behind such a hybridization is to obtain an RBF which utilizes merits of the two different types of RBFs, while compensating for the limitations of each, and keeping the formulation of a standard RBF method.

In this paper, we propose a comparatively stable local differential quadrature meshless procedure using a subdomain having 55 points, instead of the whole domain. We have utilize both integrated RBF [24, 27, 33] and hybrid RBF [46] in the local setting. The RBFs are augmented with a linear polynomial on both uniform and scattered nodes. The local meshless differential quadrature procedure is employed on given stencils at the interface, interior and outer boundary regions. The meshless method with different RBFs is tested on challenging problems having geometric singularity, oscillatory behaviour in the domains and interfaces having sharp corners.

Accuracies of the meshless methods are tested and compared for different test problems. To the best of our knowledge, such a study has not been carried out before.

2 Numerical method

In this section we describe the types of RBFs used for approximation, the stencil design at the interface, the node generation, the overall construction of the meshless method on the overlapping small stencils and the different types of interfaces.

2.1 Radial basis functions

In the RBF approximation process, the basis function $\phi(r)$ used in the approximation is dependent on some given norm of the form $r = \|\mathbf{x} - \mathbf{x}_j\|$ for some nodal point \mathbf{x}_j . Generally, RBFs can be categorized into three main classes. Firstly, compactly supported and finitely smooth RBFs. Secondly, finitely smooth global RBFs, and thirdly infinitely differentiable global RBFs with a free shape parameter such as the multiquadric (MQ) RBF. The MQ RBF has been very popular in applications due to its comparatively robust behaviour in relation to the shape parameter. The MQ RBF is defined as

$$\phi_1(r) = \sqrt{1 + (\epsilon r)^2} \quad (2)$$

where $r = \|\cdot\|_2$ is the Euclidean norm, and ϵ is the shape parameter, which controls the shape of the function. Similarly, the six times integrated MQ RBF with respect to r is given below [33]

$$\begin{aligned} \phi_2(r) = \frac{1}{201600\epsilon^6} & \left(\sqrt{1 + (\epsilon r)^2} \{40(\epsilon r)^6 - 1518(\epsilon r)^4 + 1779(\epsilon r)^2 - 128\} \right. \\ & \left. + 105\epsilon r \sinh^{-1}(\epsilon r) \{8(\epsilon r)^4 - 20(\epsilon r)^2 + 5\} \right), \end{aligned} \quad (3)$$

where ϵ is the shape parameter.

A detailed discussion about the integrated MQ RBF (3) and other integrated forms of RBFs can be found in [33]. Meshless methods based on the RBF (3) are generally poorly conditioned for small values of the shape parameter ϵ but for smooth functions, most accurate as well. As reported in [24, 33], accuracy-wise performance of the integrated RBF (3) is better than the conventional RBF (2) over a wide range of shape parameters values. Though the integrated MQ RBF (3) is comparatively less sensitive to the shape parameter than MQ RBF (2), the ill-conditioning cannot be completely decoupled from the approximation procedure due to large size global matrix.

We use the localized versions of both the integrated MQ RBF (3) and the conventional MQ RBF (2) for the construction of the proposed meshless procedure. This alteration in the method pays dividends in terms of a well conditioned matrix, and reasonable accuracy and efficiency, versus the global RBF methods and FEM. We also use the localized version of the recently reported hybrid Gaussian-Cubic RBF [46] for the numerical solution of the interface PDEs in localized setting.

The hybrid RBF has shown promising convergence properties for the numerical solution of PDE models having no interface conditions (single phase phenomenon) in the recent reported work [46]. We localize the hybrid RBF and appended a linear polynomial. As a result, the hybrid RBF performs comparatively better in the context of interface problems. The hybrid RBF in the form of Gaussian and cubic RBFs is given as

$$\phi_3(r) = \exp(-(\epsilon r)^2) + \gamma r^3 \quad (4)$$

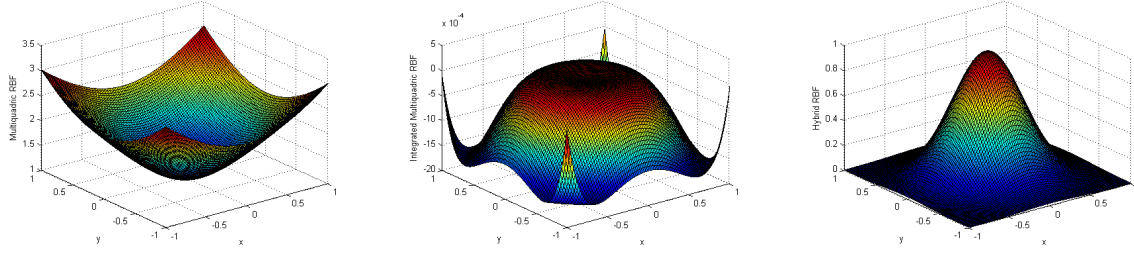


Figure 1: Surface plots of the Multiquadric (2), integrated Multiquadric (3) and Hybrid (4) RBF, respectively. (For interpretation of the colours in the figure(s), the reader is referred to the web version of this article.)

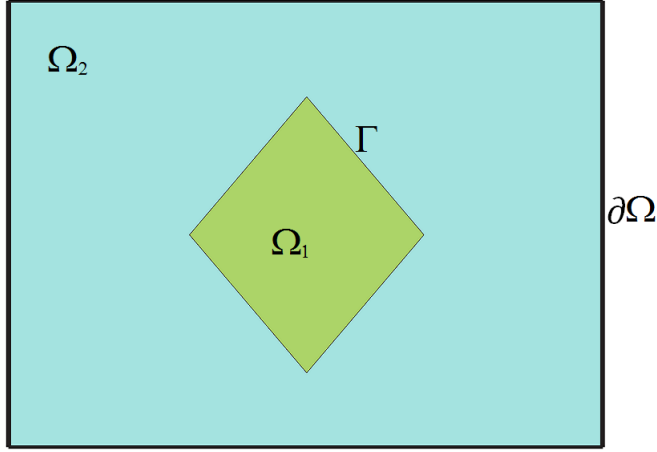


Figure 2: The domain Ω , its subregions Ω_1 and Ω_2 , the domain boundary $\partial\Omega$ and the interface Γ .

The hybrid RBF has two parameters ϵ and γ , which control accuracy and stability of the meshless method. Surface plots of Multiquadric, integrated Multiquadric and hybrid RBFs are given in Fig. 1, which reveal the radial symmetry of the basis functions.

2.2 The local meshless method

The local meshless differential quadrature procedure, also known as the RBF-FD method is implemented on local stencils defined over uniform and scattered nodal points. For two-dimensional steady state interface PDEs, we sub-divide the set of nodes $\mathbf{x}_i = (x_i, y_i)$, $i = 1, \dots, N$ in the computational domain into the following subsets (see Fig. 2):

$$\begin{aligned}\xi_1 &= \{\mathbf{x}_i \in \partial\Omega\}, \\ \xi_2 &= \{\mathbf{x}_i \in \Omega_1\}, \\ \xi_3 &= \{\mathbf{x}_i \in \Gamma\}, \\ \xi_4 &= \{\mathbf{x}_i \in \Omega_2\}.\end{aligned}\tag{5}$$

The nodal points N_m , $m = 1, 2, 3, 4$, follow the natural ordering of the sets ξ_m such that $N_1 + N_2 + N_3 + N_4 = N$. We further assume that all these subsets are non-empty. In the proposed

meshless procedure, we select a set of nearest points for each given centre \mathbf{x}_j , $j = 1, \dots, N$, with respect to the Euclidean norm, after arranging the nodes in ascending order with respect to their distance from the centre.

The basic step of RBF-based differential quadrature interpolation is to approximate derivatives of the unknown functions v_i at a node point $\mathbf{x}_j \in \boldsymbol{\xi}_r$ using function values in the neighbouring points belonging to the local stencil defined around \mathbf{x}_j (see Fig. 3). We introduce a local ordering such that $\mathbf{x}_{k'}$, $k' = 1, \dots, n$, belong to the stencil around \mathbf{x}_j of size n . Also let $\boldsymbol{\alpha} = (\alpha_1, \alpha_2)$, and introduce the notation $v_i^{(\boldsymbol{\alpha})} = \frac{\partial v_i^{(\alpha_1 + \alpha_2)}}{\partial x^{\alpha_1} \partial y^{\alpha_2}}$. Then

$$v_i^{(\boldsymbol{\alpha})}(\mathbf{x}_j) \approx \sum_{k'=1}^n \lambda_{jk'}^{(\boldsymbol{\alpha})} v_i(\mathbf{x}_{k'}) + \zeta_1 + \zeta_2 x_{k'} + \zeta_3 y_{k'}, \quad (6)$$

with the constraints

$$\sum_{k'=1}^n \lambda_{jk'}^{(\boldsymbol{\alpha})} = \sum_{k'=1}^n \lambda_{jk'}^{(\boldsymbol{\alpha})} x_{k'} = \sum_{k'=1}^n \lambda_{jk'}^{(\boldsymbol{\alpha})} y_{k'} = 0,$$

where $\lambda_{jk'}^{(\boldsymbol{\alpha})}$, ζ_1 , ζ_2 and ζ_3 are coefficients to determine. We do this by requiring the approximation (6) to be exact at \mathbf{x}_j for each of the radial basis functions centred at the stencil node points. This leads to the following set of equations

$$\phi_{i'}^{(\boldsymbol{\alpha})}(\mathbf{x}_j) = \sum_{k'=1}^n \lambda_{jk'}^{(\boldsymbol{\alpha})} \phi_{i'}(\mathbf{x}_{k'}) + \zeta_1 + \zeta_2 x_{k'} + \zeta_3 y_{k'}, \quad i' = 1, \dots, n, \quad (7)$$

$$\sum_{k'=1}^n \lambda_{jk'}^{(\boldsymbol{\alpha})} = \sum_{k'=1}^n \lambda_{jk'}^{(\boldsymbol{\alpha})} x_{k'} = \sum_{k'=1}^n \lambda_{jk'}^{(\boldsymbol{\alpha})} y_{k'} = 0, \quad (8)$$

where $\phi_j(\mathbf{x}_i) = \phi(\|\mathbf{x}_i - \mathbf{x}_j\|_2)$. We can write this as the following linear system for the stencil weights:

$$\mathbf{A}_j \boldsymbol{\lambda}_j^{(\boldsymbol{\alpha})} = \boldsymbol{\phi}_j^{(\boldsymbol{\alpha})}, \quad (9)$$

where the matrix

$$\mathbf{A}_j = \begin{bmatrix} \mathbf{A}1_j & \mathbf{P}_j \\ \mathbf{P}_j^T & \mathbf{0} \end{bmatrix},$$

$\mathbf{A}1_j$ has elements $a_{i'k'} = \phi_{i'}(\mathbf{x}_{k'})$, $i', k' = 1, \dots, n$,

$$\mathbf{P}_j^T = \begin{bmatrix} 1 & 1 & 1 & \dots & 1 \\ x_1 & x_2 & x_3 & \dots & x_n \\ y_1 & y_2 & y_3 & \dots & y_n \end{bmatrix},$$

and the vector $\boldsymbol{\lambda}_j^{(\boldsymbol{\alpha})} = (\lambda_{j1}^{(\boldsymbol{\alpha})}, \dots, \lambda_{jn}^{(\boldsymbol{\alpha})}, \zeta_1, \zeta_2, \zeta_3)^T$, and $\boldsymbol{\phi}_j^{(\boldsymbol{\alpha})} = (\phi_1^{(\boldsymbol{\alpha})}, \dots, \phi_n^{(\boldsymbol{\alpha})}, 0, 0, 0)^T$. Note that the local indexing associated with the stencil is used here. A linear system of the type above needs to be solved for each derivative operator and each node point. The matrices \mathbf{A}_j are non-singular for some choices of RBFs including the MQ RBF, as long as the involved node points are distinct. We can therefore safely express the weights as

$$\boldsymbol{\lambda}_j^{(\boldsymbol{\alpha})} = \mathbf{A}_j^{-1} \boldsymbol{\phi}_j^{(\boldsymbol{\alpha})}. \quad (10)$$

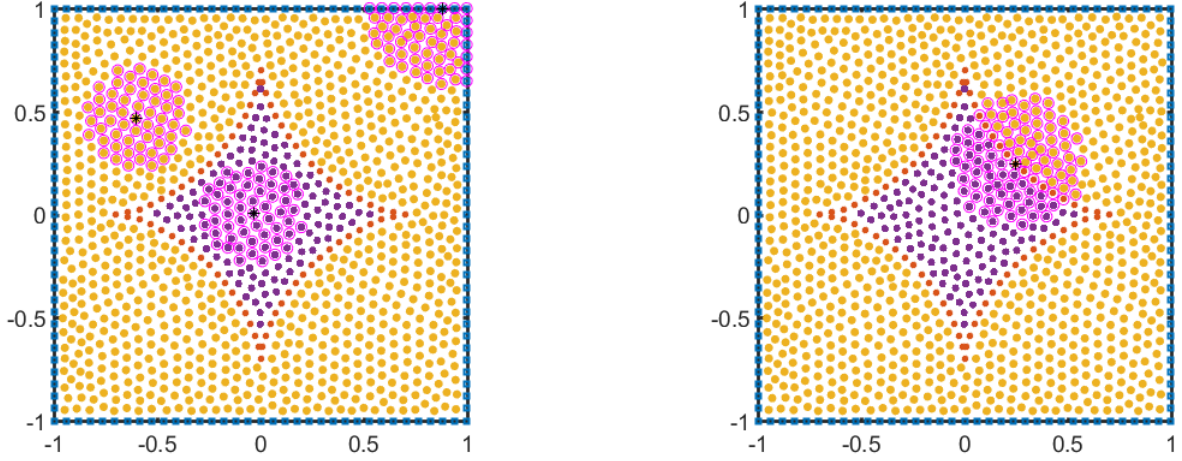


Figure 3: Selection of stencils in the subregions Ω_1 , Ω_2 , $\partial\Omega$ and the interface Γ .

We can now use these expressions to construct weights that represent the whole PDE operator defined in equations (1a)–(1b)

$$\lambda_j^{(\mathcal{L})} = \beta_l \left(\lambda_j^{(2,0)} + \lambda_j^{(0,2)} \right) + \beta_l^{(1,0)} \lambda_j^{(1,0)} + \beta_l^{(0,1)} \lambda_j^{(0,1)} - k_l e_1, \quad l = 1, 2, \quad (11)$$

where e_1 is the vector with one in the first position and zeros otherwise. Similarly, we can define weights for the derivative operators in the interface conditions as

$$\lambda_j^{(\mathcal{B})} = \beta_l \left(\lambda_j^{(1,0)} n_x + \lambda_j^{(0,1)} n_y \right), \quad l = 1, 2, \quad (12)$$

where the unit normal vector $\mathbf{n}_l = (n_x, n_y)$.

When we assemble the global matrix, we form one equation for each node point \mathbf{x}_j in the domain. We compute the local stencil weights associated with the node point and combine them into the desired operator. Then we need to convert the local indices $k' = 1, \dots, n$ to the corresponding locations in the global vector of unknowns, and then place the weights in the correct columns of the matrix. To illustrate the structure of the global matrix, we divide the contributions into blocks. Let \mathbf{B}_{qr} be the part of the assembled PDE operator with weights from (11) with rows corresponding to centre nodes $\mathbf{x}_j \in \xi_q$ and columns corresponding to weights applied to function values in nodes $\mathbf{x}_k \in \xi_r$. Similarly, the matrix block \mathbf{C}_{qr} corresponds to the interface operator with weights from (12). If we let \mathbf{I}_k represents the unit matrix of size k , and let blocks with zeros be of appropriate sizes, we can write the global system of equations as

$$\begin{bmatrix} \mathbf{I}_{N_1} & \mathbf{0} & \mathbf{0} & \mathbf{0} & \mathbf{0} \\ \mathbf{B}_{21} & \mathbf{B}_{22} & \mathbf{B}_{23} & \mathbf{0} & \mathbf{0} \\ \mathbf{0} & \mathbf{0} & \mathbf{I}_{N_3} & -\mathbf{I}_{N_3} & \mathbf{0} \\ \mathbf{0} & \mathbf{C}_{32} & \mathbf{C}_{33} & -\mathbf{C}_{33} & -\mathbf{C}_{34} \\ \mathbf{0} & \mathbf{0} & \mathbf{0} & \mathbf{B}_{43} & \mathbf{B}_{44} \end{bmatrix} \begin{bmatrix} v_1(\xi_1) \\ v_1(\xi_2) \\ v_1(\xi_3) \\ v_2(\xi_3) \\ v_2(\xi_4) \end{bmatrix} = \begin{bmatrix} h(\xi_1) \\ f_1(\xi_2) \\ g_1(\xi_3) \\ g_2(\xi_3) \\ f_2(\xi_4) \end{bmatrix} \quad (13)$$

The global coefficient matrix of the system (13) is sparse and non-symmetric, with n non-zero elements per row for equations corresponding to interior node points, and with $2n$ non-zero elements in the rows corresponding to the derivative interface conditions. This greatly reduces the computational cost compared to the global meshless method. The system of linear equations can be solved by a direct method or by an iterative method.

3 Numerical results and discussion

In this section, the proposed local meshless methods are tested for accuracy on a range of two-dimensional elliptic interface problems for the interface boundaries shown in Table 1. The notation LMM1P is used for the local meshless method based on the ϕ_1 RBF, LMM2P for the local meshless method based on the ϕ_2 RBF and LMM3P for the local meshless method based on the ϕ_3 RBF. We augmented each the respective RBF with a linear polynomial. Both uniform and scattered nodes are considered for the test Problem 1, 2, 3, 4 and 9 for the purpose of comparisons with the published work. In the test Problems 5, 6, 7, and 8, where there is no comparison, only scattered nodes are used.

To generate a set of scattered node, we first select a global approximate nodal distance h . Afterwards, we place the nodes uniformly on each segment of the outer boundary and the interface. In this way, we make sure the placement of nodes at all corner points. The subdomains Ω_1 and Ω_2 are initially filled with nodes using node placing algorithm described in [47]. The nodes that are closer than $h/4$ to the boundary or interface are pruned, and then finally a few iterations of an electrostatic node repulsion algorithm are applied to the interior nodes in each subdomain, while the boundary and interface nodes stay fixed. Examples of the generated node distributions are shown in Fig. 4 (having $h = 0.06$). In case of the uniform rectangular nodes, the nodal distance h is defined as $2/N_x$, where N_x is the total number of nodes on x -axis. Since the unit normal vectors of the nodes lying on the sharp corners are undefined, therefore, the unit normal vectors of the adjacent immediate neighbour nodes are considered.

The right hand side of (1) and other necessary information are taken from the exact solution given in each benchmark problem. The number of points in each local support domain is kept fixed at $n = 55$. Value of the shape parameter in the method LMM2P is kept fixed at 6, while in the methods LMM1P and LMM3P its value is kept fixed at 2 unless stated otherwise. Similarly, coefficient γ of the cubic spline in (4) is taken 10^{-6} .

For test Problem 1, sensitivity of all the methods versus the shape parameter is also investigated in the interval $\epsilon \in [0.5, 7]$. Different types of interfaces with sharp corners are shown in Table 1 and Fig. 4 together with the layout of scattered nodes. The values of $k_1 = k_2 = 0$ are used for all the test problems except the test problem 8, where the non-zero values are mentioned.

Surface plots of the numerical solution obtained through the LMM2P are shown for each benchmark problems. We do not include surface plots for the methods, since they are qualitatively similar. For the error measurements, L_∞ error norm is used. All the numerical experiments are performed on a Laptop Intel Core I7 with 8 GB RAM.

Test Problem 1 ([16]). We consider elliptic interface problem (1) with a Star-shaped interface. Such type of interface has a geometric singularity. It is important to know, whether the local meshless methods can handle complex and non-smooth interfaces on uniform or scattered nodes accurately. For this we let [16]

$$\beta = \begin{cases} 1 & \text{in } \Omega_1, \\ 2 + \sin(x + y) & \text{in } \Omega_2. \end{cases}$$

Table 1: The equations describing the (non-smooth) interface curves.

Type of interface	Equation
Star [16]	$x = r \cos(\theta),$ $y = r \sin(\theta),$ where $r = \frac{R \sin(\theta_t/2)}{\sin(\theta_t/2 + \theta - \theta_r - 2(\theta_i - 1)\pi/5)},$ if $\theta_r + (2\theta_i - 2)\pi/5 \leq \theta < \theta_r + (2\theta_i - 1)\pi/5,$ $r = \frac{R \sin(\theta_t/2)}{\sin(\theta_t/2 - \theta + \theta_r + 2(\theta_i - 1)\pi/5)},$ if $\theta_r + (2\theta_i - 3)\pi/5 \leq \theta < \theta_r + (2\theta_i - 2)\pi/5,$ $R = 6/7, \theta_t = \pi/5, \theta_r = \pi/7$ and $\theta_i = 1, 2, 3, 4, 5$
Half lemniscate	$x = 1.2 \cos(2\theta) \cos(\theta) + 1,$ $y = 1.2 \cos(2\theta) \sin(\theta), \quad 3\pi/4 \leq \theta \leq 5\pi/4$
Astroid	$x = 0.65 \cos^3(\theta),$ $y = 0.65 \sin^3(\theta), \quad 0 \leq \theta \leq 2\pi$
Deltoid	$x = 0.3(2 \cos(\theta) + \cos(2\theta)),$ $y = 0.3(2 \sin(\theta) - \sin(2\theta)), \quad 0 \leq \theta \leq 2\pi$
Hypocycloid	$x = 0.06(8 \cos(\theta) + 2 \cos(4\theta)),$ $y = 0.06(8 \sin(\theta) - 2 \sin(4\theta)), \quad 0 \leq \theta \leq 2\pi$
Epicycloid	$x = 0.05(9 \cos(\theta) + \cos(9\theta)),$ $y = 0.05(9 \sin(\theta) - \sin(9\theta)), \quad 0 \leq \theta \leq 2\pi$

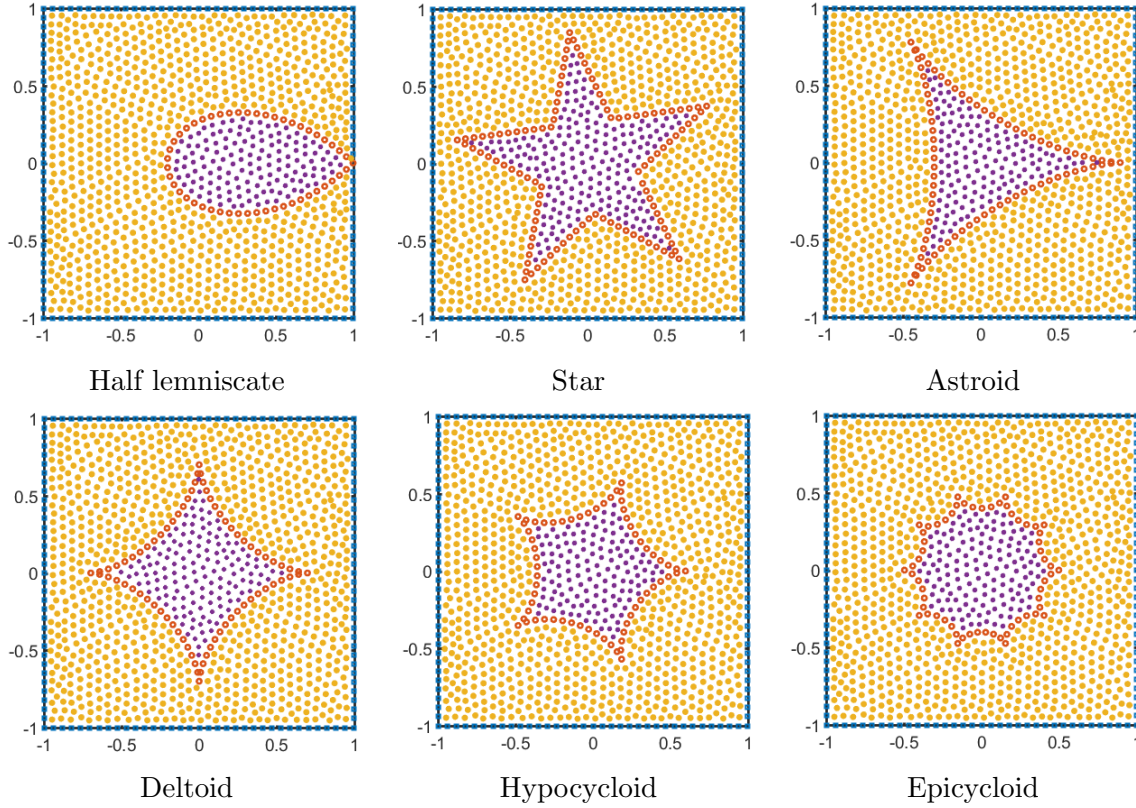


Figure 4: The computational domains with sample node distributions for different interface shapes given in Table 1.

Table 2: Comparison of the local meshless methods with numerical results in [16] for Test Problem 1.

$N_x \times N_y$	LMM1P	LMM2P	LMM3P	Courtesy ([16])
20×20	1.74e-02	4.16e-04	1.00e-02	4.08e-03
40×40	1.13e-04	5.75e-06	6.17e-05	1.13e-03
80×80	2.01e-05	1.03e-06	1.96e-05	3.12e-04

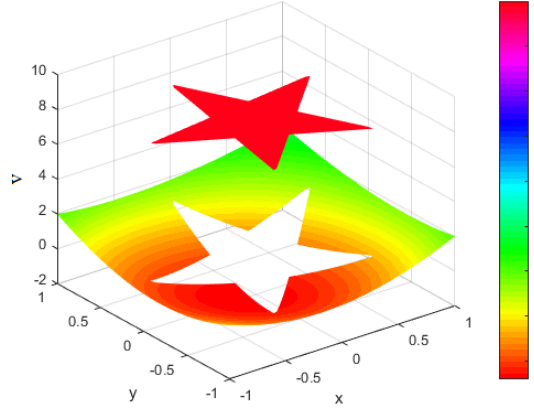


Figure 5: Surface plot of the numerical solution for Test Problem 1.

Analytical solution of the problem is given by

$$v(x, y) = \begin{cases} 8 & \text{in } \Omega_1, \\ x^2 + y^2 + \sin(x + y) & \text{in } \Omega_2. \end{cases} \quad (14)$$

Numerical results for test Problem 1 are displayed in Tables 2, Fig. 5 and Fig. 6. Fig. 5 shows a jump in the numerical solution by LMM2P. N_x and N_y represent the number of nodes in the x -direction and y -direction, respectively. Fig. 6 shows a comparison of the proposed meshless methods on scattered interior nodes as well as on uniform nodes. The number of nodes on the boundary and on the interface increases while increasing the number of interior nodes. The shape parameter ϵ is taken 6 in the case of LMM2P and 2 for the methods LMM1P and LMM3P. In Table 2, a comparison of accuracy of the methods LMM1P, LMM2P and LMM3P is made with method [16]. Table 2 shows that the LMM2P performs marginally better due to a higher rate of convergence, where as performance of the LMM3P is good as well.

From Fig. 6, we can conclude that accuracy of the meshless method LMM2P is better than the other proposed methods. The numerical solution of the LMM2P converges faster to the exact solution both on scattered and uniform nodes. The rate of convergence of the LMM2P on scattered nodes is 3.9 and on uniform nodes it is 5.2. The numerical solutions of the LMM1P and the LMM3P are also in good agreement with exact solution on both types of nodal arrangements. The order of convergence of the LMM1P on scattered nodes is 3.5 and on uniform nodes it is 4.2. Similarly, the order of convergence of the LMM3P on scattered nodes is 1.4 and in case of uniform nodes it is 2.9. The condition numbers κ of the proposed meshless methods are comparable for coarser nodes. However, for dense nodes, the condition number of LMM1P is higher than the

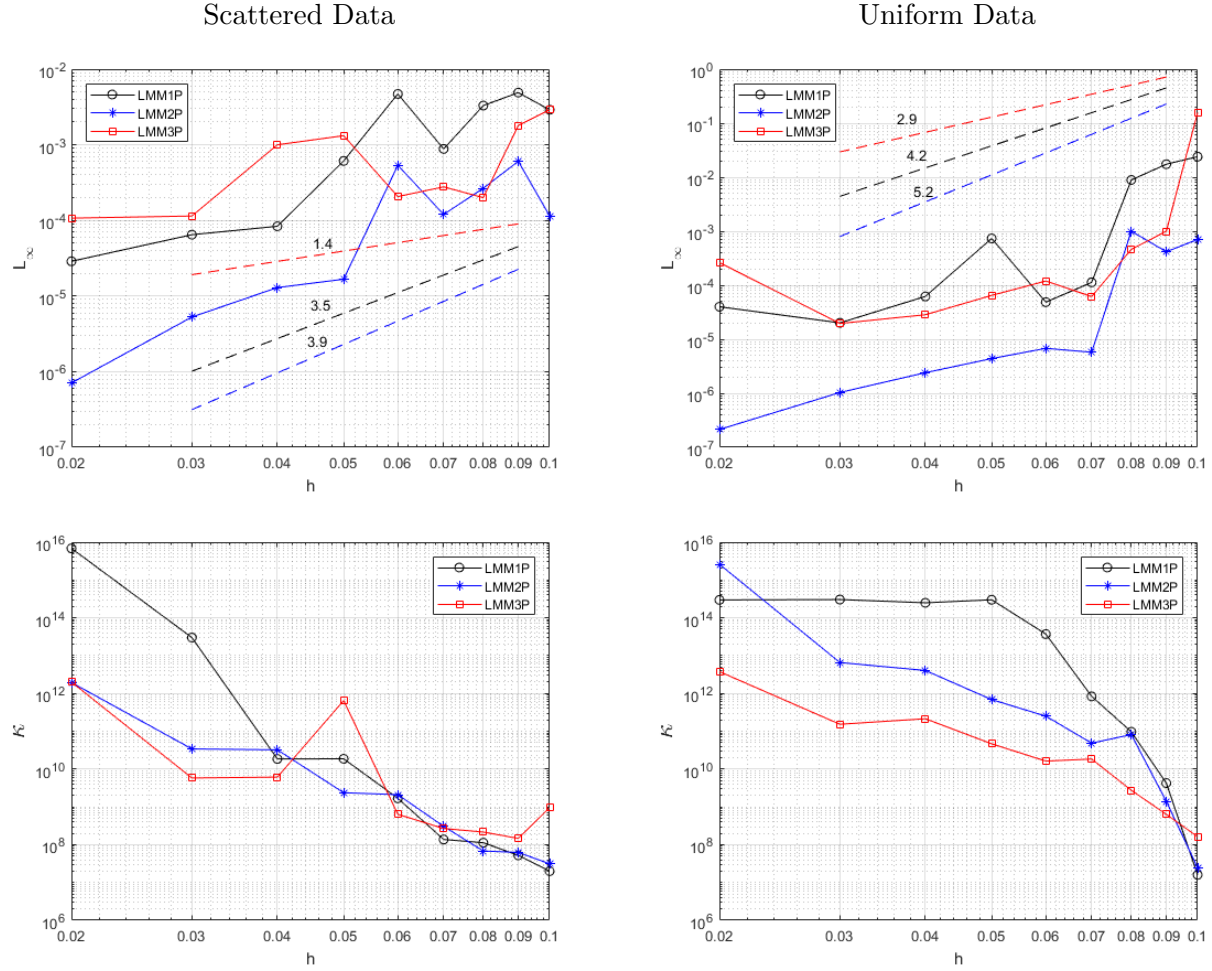


Figure 6: Errors and κ as a function of h for Test Problem 1.

methods LMM2P and LMM3P.

We have included two graphs in Fig. 6 for both scattered and uniform nodes showing the condition numbers of the resulting linear system versus the nodes of the proposed methods. The condition numbers of the proposed algorithm increase with the increase in the nodal points. The method LMM3 has comparatively small condition number.

Dependency of the accuracies of the proposed methods on the shape parameter ϵ , when it is chosen in the interval $[1, 5]$, are shown in Fig. 7. The number of scattered points used in this experiment is 1482. The figure shows an increasing trend in the error with increasing shape parameter values for all of the methods. The LMM2P exhibits comparatively better accuracy for the given range. A theoretical frame work to find the optimum value of the shape parameter is still lacking, though there exists some optimization procedure like the one based on the golden search algorithm [48, 49] and some other evolutionary optimization techniques, which are currently in practice. We did not use them in order to keep the cost of the algorithm low. In contrast to global meshless methods, shape parameter sensitivity of the proposed local meshless methods is substantially smaller. When the shape parameter value is changed from 1 to 5, accuracy range of the LMM1P varies in 10^{-4} to 10^{-1} . Similarly, accuracy wise variation of the LMM2P is 10^{-5} to 10^{-7} , whereas that of the LMM3P, accuracy varies in the range 10^{-2} to 10^{-4} .

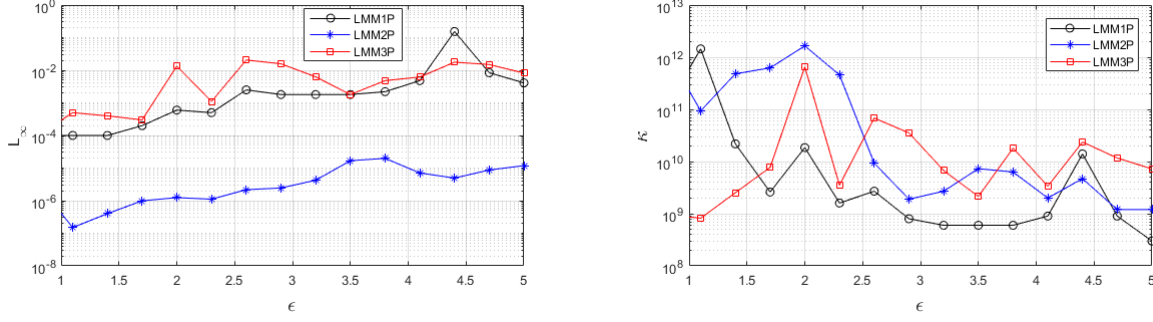


Figure 7: Shape parameter dependency investigation for Test Problem 1.

Table 3: Comparison of the local meshless methods with MIB Galerkin [50] for Test Problem 2.

$N_x \times N_y$	LMM1P	LMM2P	LMM3P	Courtesy ([50])
20×20	11.056	9.857	2.5124	7.25e-01
40×40	8.74e-02	2.67e-02	3.01e-01	1.68e-01
80×80	8.05e-04	1.74e-04	2.20e-03	4.43e-02

Test Problem 2 ([50]). We consider the 2D Poisson equation in the domain $[-1, 1] \times [-1, 1]$, carrying additional challenge of oscillatory behaviour in the outer sub-domain. Discontinuity in the coefficient is given by

$$\beta = \begin{cases} 5 & \text{in } \Omega_1, \\ 3 & \text{in } \Omega_2. \end{cases}$$

Analytical solution of the problem is given by

$$v(x, y) = \begin{cases} 7 + x^2 + y^2 & \text{in } \Omega_1, \\ \sin(3\pi x) \sin(3\pi y) & \text{in } \Omega_2. \end{cases} \quad (15)$$

MIB Galerkin method [50] has been reported to deal with the numerical solution of the PDEs with complicated non-smooth interfaces, having partly oscillatory behaviour. The proposed methods LMM1P, LMM2P, and LMM3P are implemented on uniform nodes for the purpose of comparison as shown in Table 3. The obvious advantage of the proposed methods is their flexibility in the selection of the nodes. It is clear from Tables 3 that accuracy-wise performance of the MIB Galerkin method [50] is lower than that of the proposed local meshless methods. The methods LMM1P and LMM2P perform better than the other counter part methods.

Surface plot of the numerical solution produced by the method LMM2P is shown in Fig. 8. Fig. 9 shows a comparison of all the proposed meshless methods LMM1P, LMM2P and LMM3P. Values of the shape parameter are taken similar to the previous problem. It can be seen from Fig. 9 that the L_∞ error norm decreases with decreasing nodal distance h , and accuracies of the proposed methods are comparable for scattered and uniform nodes. In the present problem, the LMM2P has higher order of convergence than the methods LMM1P and LMM3P. Condition numbers (κ) of the LMM3P is better than the LMM1P and the LMM2P on both type of nodes as shown in Fig. 9.

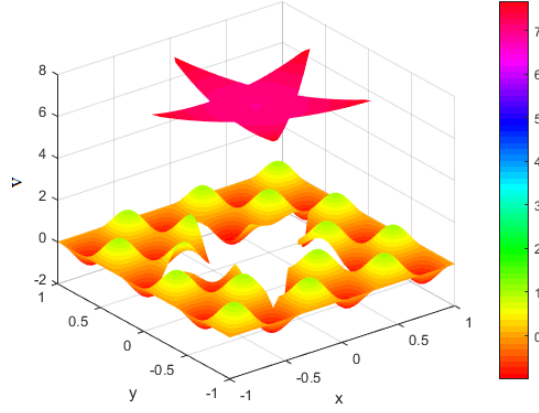


Figure 8: Surface plot of the numerical solution for Test Problem 2.

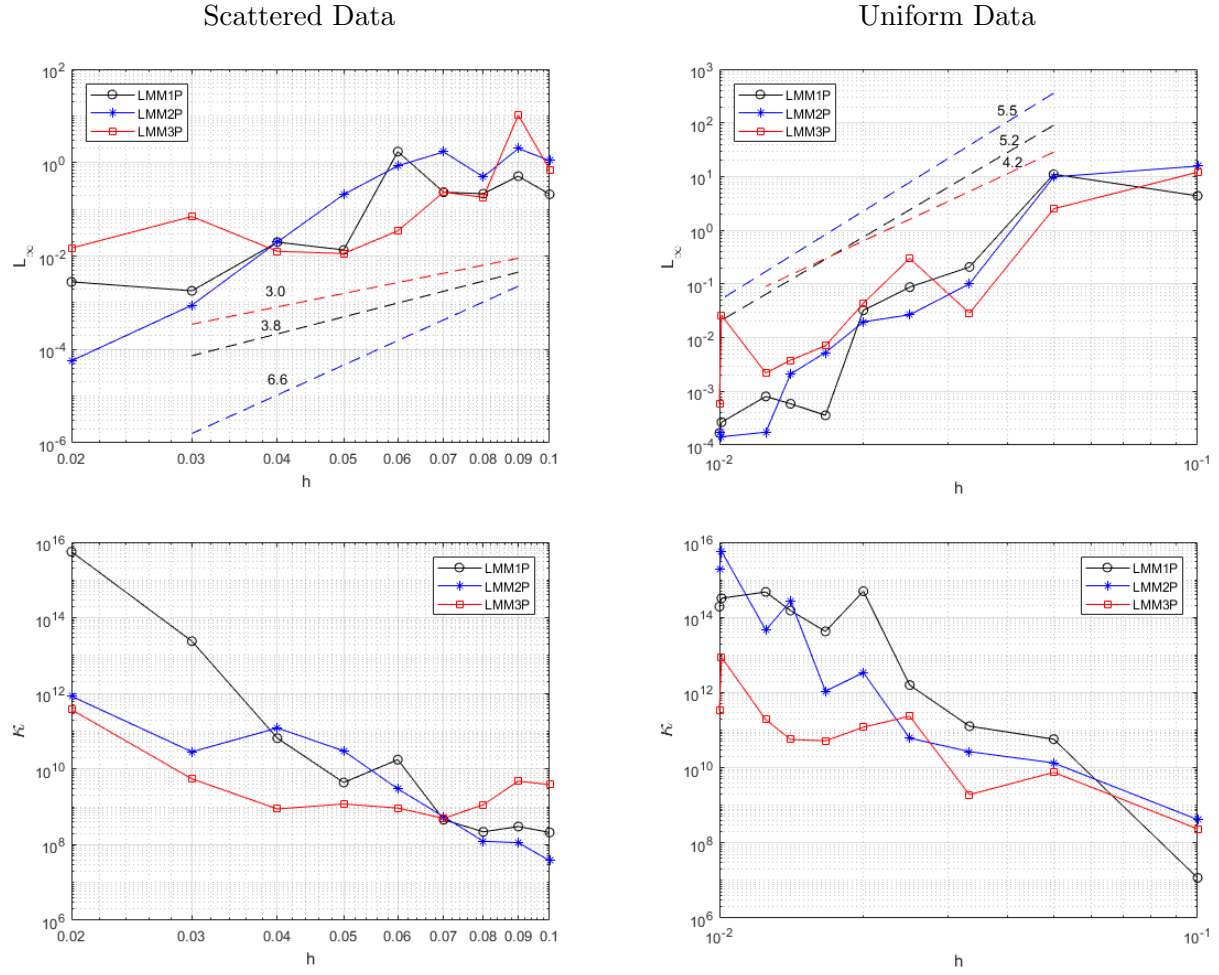


Figure 9: Errors and κ as a function of h for Test Problem 2.

Table 4: Comparison of the local meshless methods with MIB Galerkin [50] for Test Problem 3.

$N_x \times N_y$	LMM1P	LMM2P	LMM3P	Courtesy ([50])
20×20	2.80e-02	3.89e-02	1.98e-01	7.25e-01
40×40	2.73e-03	8.75e-03	5.00e-02	1.68e-01
80×80	3.61e-03	1.52e-03	7.10e-03	4.43e-02

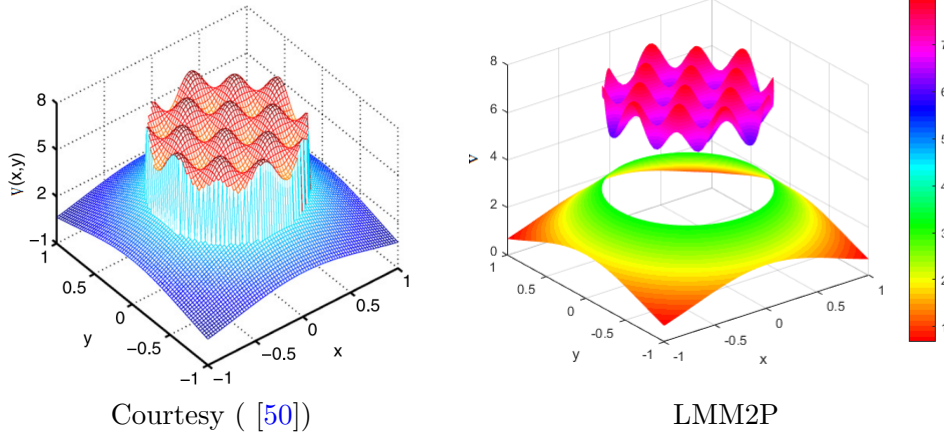


Figure 10: Surface plots of the numerical solution for Test Problem 3.

Test Problem 3 ([50]). We consider a 2D interface Poisson equation in the computational domain $[-1, 1] \times [-1, 1]$ having an oscillatory solution in the interior sub-domain. The interface is a circle of radius $r = 2/3$. The discontinuous coefficient is given by

$$\beta = \begin{cases} 2 & \text{in } \Omega_1, \\ 3 & \text{in } \Omega_2. \end{cases}$$

Analytical solution of the problem is given by

$$v(x, y) = \begin{cases} 7 + \sin(4\pi x) \sin(4\pi y) & \text{in } \Omega_1, \\ 5 \exp(-x^2 - y^2) & \text{in } \Omega_2. \end{cases} \quad (16)$$

The L_∞ error norms of the methods LMM1P, LMM2P, LMM3P and MIB Galerkin method [50] are shown in Tables 4. The methods LMM1P, LMM2P and LMM3P perform better than MIB Galerkin method for this test problem. The L_∞ error norms of the methods LMM1P and LMM2P are slightly better than the LMM3P. Surface plots of the numerical solutions produced by the LMM2P are shown in Fig. 10. Fig. 11 shows the L_∞ error norm and condition numbers κ of the proposed methods versus the scattered nodes. The LMM2P performs better than the methods LMM1P and LMM3P, with 4.7 order of convergence. The orders of convergence of LMM1P and LMM3P are approximately same in the present test problem. The condition numbers κ of the proposed methods are comparable in case of coarser scattered nodes, while the condition numbers of the LMM1P are higher as compared to the LMM2P and the LMM3P in case of dense scattered nodes.

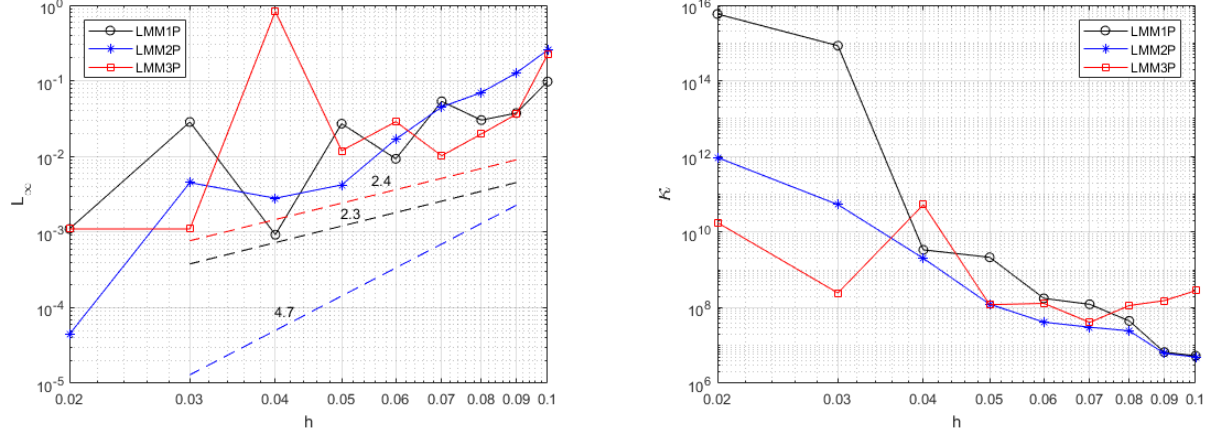


Figure 11: Errors and κ as a function of h for Test Problem 3.

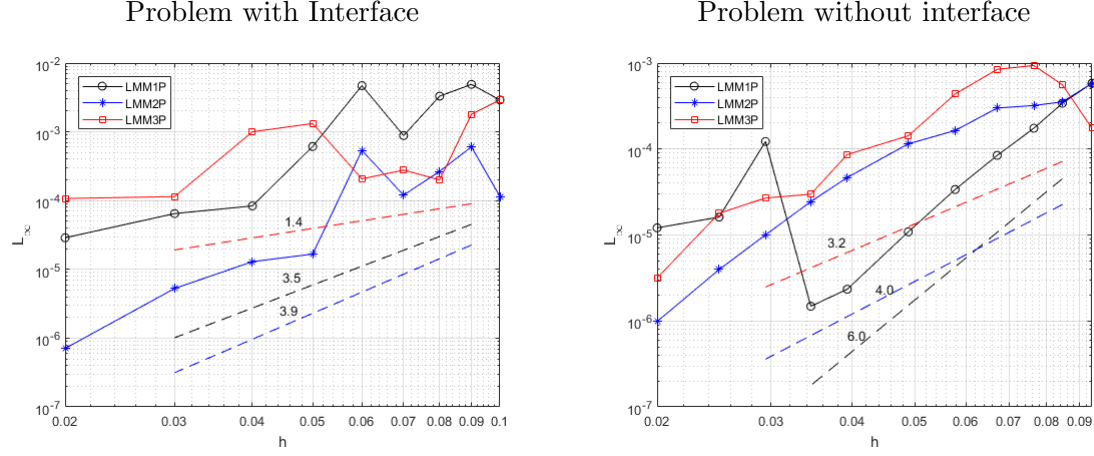


Figure 12: Errors as a function of h for Test Problem 4.

Test Problem 4. In this case, we focus on accuracy-wise performance of the proposed meshless methods with and without interface conditions. To this end, we undertake a comparison of the numerical results of Test Problem 1 for the following plain Poisson PDE

$$\nabla \cdot (\beta \nabla v) = f, \quad \text{in } \Omega,$$

where $\beta = 2 + \sin(x + y)$ and the function f is obtained from the following analytical solution

$$v(x, y) = x^2 + y^2 + \sin(x + y).$$

In this test case we want to analyse effects of the interface conditions on accuracy of the proposed meshless methods. Graphical illustrations are shown in Fig. 12 in terms of L_∞ error norm versus nodal distance h by taking scattered nodes. It is clear from the graphs that the numerical solutions produced by the LMM1P and the LMM3P in the case of elliptic PDE without interface conditions are slightly accurate than the numerical solutions of the elliptic PDE with interface conditions.

Numerical solution of the LMM2P is comparable in both cases. The order of convergence of the LMM2P is 4 in both the cases. The order of convergence of the LMM1P and the LMM3P for PDE without interface conditions is higher than the PDE with interface conditions. Consequently, presence of the interface phenomenon effects accuracy of the meshless methods due to heterogenous behaviour across the interface.

Test Problem 5 ([15]). Consider an elliptic interface problem (1) having half of a Lemniscate shaped interface, with one sharp corner of the interface extending to the outer boundary. Analytical solution of the problem is given by

$$v(x, y) = \frac{-y^2 + ((x-1)\tan(\theta))^2 x}{\beta(x, y)}, \quad (17)$$

where $\theta = 40$ and

$$\beta(x, y) = \begin{cases} 1 & \text{if } (x, y) \in \Omega_1, \\ 1000 & \text{if } (x, y) \in \Omega_2. \end{cases}$$

Surface plots of the numerical solution produced by the LMM2P is shown in Fig. 13. Fig. 14 shows a comparison of the proposed meshless methods. Scattered nodes are used in this case as well. It can be seen from Fig. 14 that the L_∞ error norm decreases its value in all the cases. Furthermore, accuracy of the LMM2P is better than all the other methods. The orders of convergence of the methods LMM1P, LMM2P and LMM3P are shown in the same figure. In the present case, the order of convergence of the LMM2P is better than the LMM1P and LMM3P. Condition numbers of the LMM2P and the LMM3P are comparable, However, for dense nodes, the condition numbers κ of the LMM1P are higher than the LMM2P and the LMM3P.

Test Problem 6 ([15]). The elliptic interface problem (1) with an Deltoid-like interface structure is considered. Analytical solution of the problem is given by

$$v(x, y) = \begin{cases} \frac{(x^2+y^2)^{3/2}}{\beta_1}, & \text{in } \Omega_1 \\ \frac{(x^2+y^2)^{3/2}}{\beta_2} + (\frac{1}{\beta_1} - \frac{1}{\beta_2})r_0, & \text{in } \Omega_2, \end{cases}$$

where $r_0 = 0.5$, $\beta_1 = 1$ and $\beta_2 = 1000$.

Fig. 13 shows the surface plots of the numerical solutions produced by the LMM2P. Fig. 14 shows a comparison of the proposed meshless methods. The LMM2P performs well in the comparison. The LMM1P has the worst performance in both the cases. This could be due the sensitivity effects of the shape parameter ϵ . The condition numbers κ of LMM1P is higher in case of dense nodes. While, the condition numbers κ of the LMM2P and LMM3P are comparable. The LMM2P has again better order of convergence than the LMM1P and the LMM3P. Lower accuracy can be related to inappropriate selection of the shape parameter ϵ as shown in the case of LMM1P in Fig. 14.

Test Problem 7 ([15]). The elliptic interface problem (1) with an Astroid-like interface is considered. Analytical solution of the problem is given by

$$v(x, y) = \frac{1}{\beta(x, y)} \left(\frac{x^2}{0.5^2} + \frac{y^2}{0.25^2} - 1 \right), \quad (18)$$

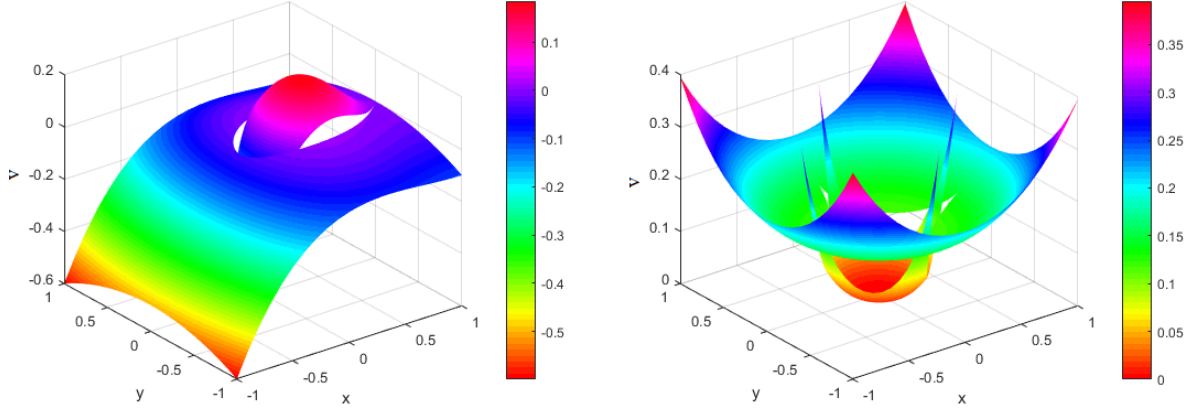


Figure 13: Surface plots of the numerical solutions for Test Problems 5 (left) and 6 (right).

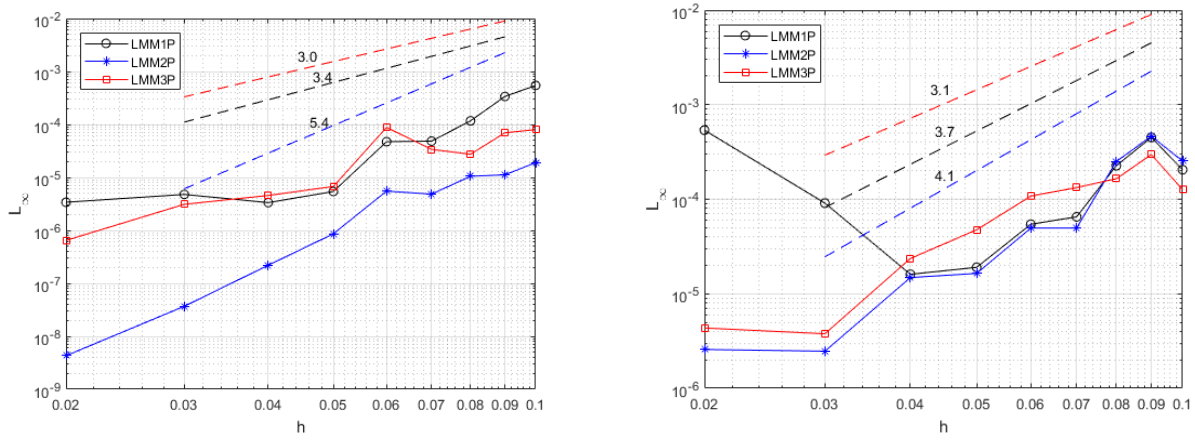


Figure 14: Errors as a function of h for Test Problems 5 (left) and 6 (right).

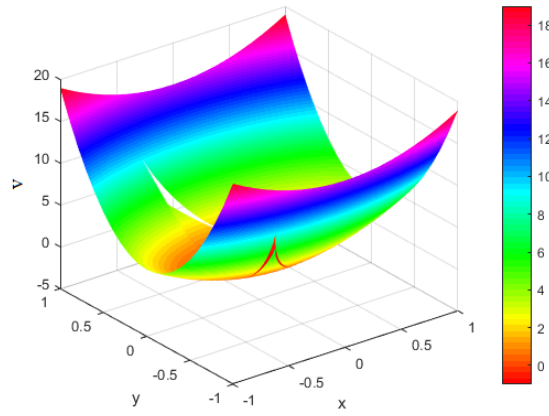


Figure 15: Surface plot of the numerical solution for Test Problem 7.

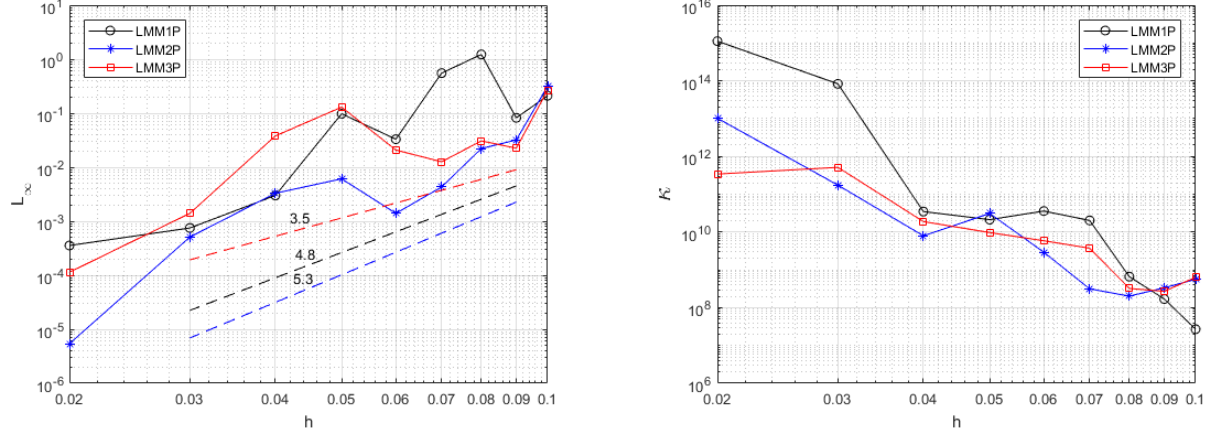


Figure 16: Errors and κ as a function of h for Test Problem 7.

where

$$\beta(x, y) = \begin{cases} 1 + 0.5(x^2 - xy + y^2) & \text{if } (x, y) \in \Omega_1, \\ b & \text{if } (x, y) \in \Omega_2. \end{cases}$$

Fig. 15 shows the numerical solutions of Test Problem 7 produced by the LMM2P. Fig. 16 shows a comparison of the proposed meshless methods. Scattered nodes are considered in all the cases. A diffusion coefficient $b = 1000$ is used. Similar behaviour of the condition number is observed in the previous experiments. However, the condition number of the LMM3P is marginally better. Keeping in view the trend of L_∞ error norm, the LMM2P converges to the exact solution with the higher order convergence as compared to the other proposed methods.

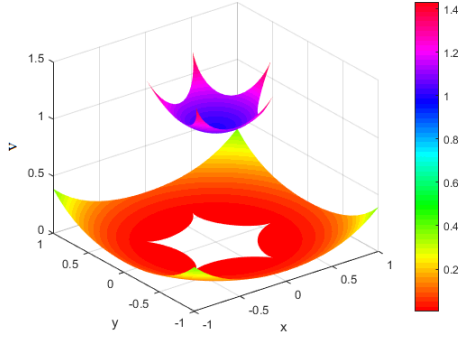
Test Problem 8 ([24]). The elliptic interface problem (1) with a Hypocycloid and Epicycloid like interfaces is considered. Analytical solution of the problem is given by

$$v(x, y) = \begin{cases} \exp(x^2 + y^2) & \text{if } (x, y) \in \Omega_1 \\ 0.1(x^2 + y^2)^2 - 0.01 \log(2\sqrt{x^2 + y^2}) & \text{if } (x, y) \in \Omega_2. \end{cases} \quad (19)$$

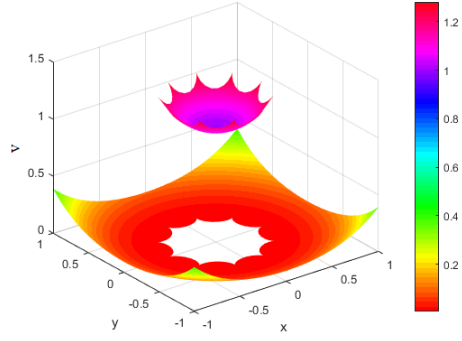
We choose $k_1 = k_2 = 10(x + y)$ and

$$\beta(x, y) = \begin{cases} 1 & \text{if } (x, y) \in \Omega^1 \\ 10 & \text{if } (x, y) \in \Omega^2. \end{cases} \quad (20)$$

Fig. 17 shows the edges of the Hypocycloid and Epicycloid in the numerical solutions produced by the LMM2P. Fig. 18 shows a comparative performance of the proposed meshless methods. The LMM2P performs well in both cases. The L_∞ error norm of the LMM2P decreases and the order of convergence of the method is approximately 4.7 in both the cases. For coarser nodes, the condition numbers of the proposed methods are comparable. But for dense nodes, the condition numbers of the LMM1P are higher than the other methods.



Hypocycloid



Epicycloid

Figure 17: Surface plots of the numerical solution for Test Problem 8.

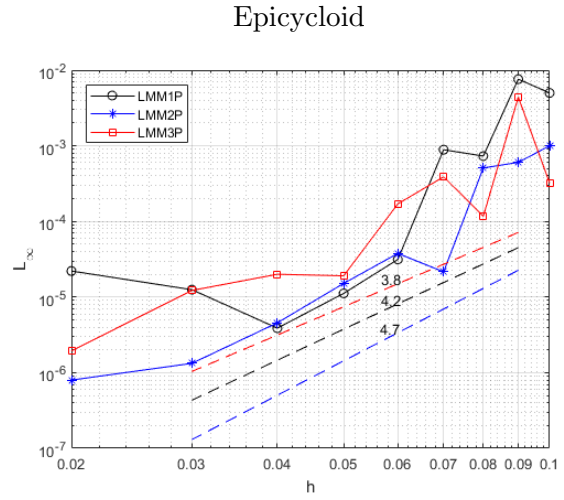
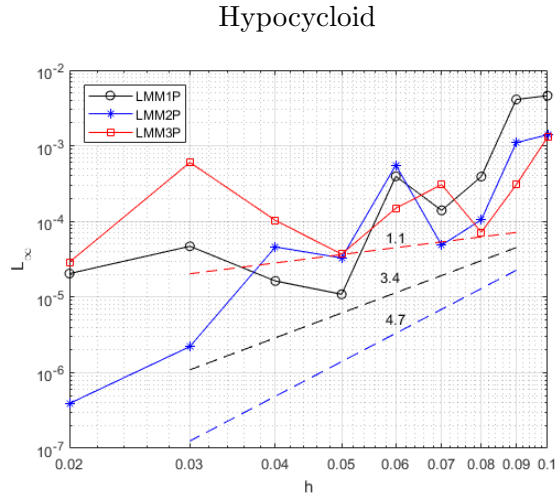


Figure 18: Errors as a function of h for Test Problem 8.

Table 5: Comparison of the local meshless methods with [22] for Test Problem 9.

$N_x \times N_y$	LMM1P	LMM2P	LMM3P	$N_x \times N_y$	Courtesy ([22])
41×21	4.13e-02	2.08e-02	2.58e-01	41×21	4.12e-02
81×41	8.93e-03	5.14e-03	4.54e-03	81×41	2.30e-02
110×81	1.65e-03	2.01e-03	5.03e-04	161×81	1.28e-02
161×81	2.37e-03	2.12e-03	9.43e-04	321×161	7.02e-03

Test Problem 9 ([22]). The elliptic interface problem (1) is considered with the following parameters and analytical solution

$$v(x, y) = \begin{cases} 8, & \text{if } (x, y) \in \Omega_1, \\ (x^2 + y^2)^{5/6} + \sin(x - y), & \text{if } (x, y) \in \Omega_2, \end{cases} \quad (21)$$

and

$$\beta(x, y) = \begin{cases} 1, & \text{if } (x, y) \in \Omega_1, \\ 2 + \sin(x + y) & \text{if } (x, y) \in \Omega_2. \end{cases}$$

The interface is defined as

$$\Gamma(x, y) = \begin{cases} y - 2x, & \text{if } x + y > 0, \\ y + 0.5x & \text{if } x + y \leq 0. \end{cases}$$

As mentioned in [22] that the interface Γ is only Lipschitz continuous and has a weak singular point at $(0, 0)$. Also the solution $v(x, y)$ has a weak singularity at $(0, 0)$, which coincides with the interface singular point. Comparison of L_∞ error norms of the methods LMM1P, LMM2P and LMM3P with [22] are shown in Table 5. Computational domain of the problem is taken $(-1, 3) \times (-1, 1)$. From the Table 5, it can be seen that accuracies of the methods LMM1P, LMM2P and LMM3P in term of L_∞ error norms are comparable with each other and are better than [22].

4 Conclusion

In the present work, we mainly investigated three types of local meshless differential quadrature (also called RBF-FD) methods for solving elliptic boundary-value interface problems with closed interfaces and corners in a square domain. We also augmented the RBFs with a linear polynomial $x+y+1$ in the localized domain. Accuracies of the methods are compared with the FEM, reported in the literature. The proposed meshless methods have dealt with a variety of complicated non-smooth interfaces through a fairly simple meshless numerical procedure. Validity of the proposed methods can further be extended to three-dimensional models with complex interfacial dynamics on non-smooth interfaces. Based on the benchmark tests, we conclude the following outcomes:

- Numerical experiments show that in most cases, performance of the method LMM2P is better than the methods LMM1P, LMM3P. Performances of the methods LMM1P and LMM3P are comparable to each other.
- Local meshless methods can handle weak geometrical singularities and oscillatory solutions in the inner and outer interface regions, accurately.
- Local meshless methods lose some accuracy in the presence of interface conditions (see Fig. 12).
- Local meshless methods perform well both on uniform data and on scattered data. Meshless methods perform better in terms of accuracy than some of the available methods in the literature.
- Unlike the conventional methods, the local meshless methods can easily be implemented on irregular interface geometries

5 Declaration of competing interest

The authors declare that they have no known competing financial interests or personal relationships that could have appeared to influence the work reported in this paper.

6 Acknowledgments

- i*). The first two authors have greatly acknowledged the Higher Education Commission of Pakistan for their support in the present work under the project No. 7870/KPK/NTPU/R&D/HEC/2017.
- ii*). We are also thankful to Slobodan Milovanović, formerly at Uppsala University, for supplying a code for node generation and electrostatic node repulsion that we could modify for the problems in this manuscript.
- iii*). We are thankful to the anonymous reviewers for their valuable comments and suggestions, which have improved the paper considerably.

References

- [1] K. Xia, M. Zhan, and G. W. Wei. MIB Galerkin method for elliptic interface problems. *Journal of Computational and Applied Mathematics*, 272:195–220, 2014.
- [2] S. Yu, Y. Zhou, and G. W. Wei. Matched interface and boundary (MIB) method for elliptic problems with sharp-edged interfaces. *Journal of Computational Physics*, 224:729–756, 2007.
- [3] R. Miniowitz and J.P. Webb. Covariant-projection quadrilateral elements for the analysis of wave-guides with sharp edges. *IEEE Trans. Microwave Theory Technology*, 39:501–505, 1991.
- [4] E.B. Macak, W.D. Munz, and J.M. Rodenburg. Plasma-surface interaction at sharp edges and corners during ion-assisted physical vapor deposition. Part I: Edge-related effects and their influence on coating morphology and composition. *Journal of Applied Physics*, 4:2829–2836, 2003.
- [5] F. Baetke, H. Werner, and H. Wengle. Numerical-simulation of turbulent-flow over surface-mounted obstacles with sharp edges and corners. *J. Wing Engng. Indust. Aerodyn*, 35:129–147, 1990.
- [6] Z.P. Tanner, J.Z. Savage, D.R. Tanner, and A.F. Peterson. Two-dimensional singular vector elements for finite-element analysis. *IEEE Trans. Microwave Theory Technology*, 46:178–184, 1998.
- [7] G. Pan, M. Tong, and B. Gilbert. Multiwavelet based moment method under discrete Sobolev-type norm. *Microwave Opt. Techn. Lett.*, 40:47–50, 2004.
- [8] L. Mu, J. Wang, G. Wei, X. Ye, and S. Zhao. Weak Galerkin methods for second order elliptic interface problems. *Journal of Computational Physics*, 250:106–125, 2013.
- [9] J. S. Chen, L. Wang, H. Y. Hu, and S. W. Chi. Subdomain radial basis collocation method for heterogeneous media. *International Journal for Numerical Methods in Engineering*, 80:163–190, 2009.

- [10] J. Albright, Y. Epshteyn, M. Medvinsky, and Q. Xia. High-order numerical schemes based on difference potentials for 2D elliptic problems with material interfaces. *Applied Numerical Mathematics*, 111:64–91, 2017.
- [11] D. Appelö and N. A. Petersson. A stable finite difference method for the elastic wave equation on complex geometries with free surfaces. *Communications in Computational Physics*, 5(1):84–107, 2009.
- [12] J. Bedrossian, J. V. Brecht, Zhu, E. Sifakis, and J. M. Teran. A second order virtual node method for elliptic problems with interfaces and irregular domains. *Journal of Computational Physics*, 229(18):6405–6426, 2010.
- [13] A. Guittet, M. Lepilliez, S. Tanguy, and F. Gibou. Solving elliptic problems with discontinuities on irregular domains—the Voronoi Interface Method. *Journal of Computational Physics*, 298:747–765, 2015.
- [14] j. E. Kozdon and L. C. Wilcox. Stable coupling of nonconforming, high-order finite difference methods. *SIAM Journal on Scientific Computing*, 38(2):A923–A952, 2016.
- [15] H. Guo and X. Yang. Gradient recovery for elliptic interface problem: II. Immersed finite element methods. *Journal of Computational Physics*, 338:606–619, 2017.
- [16] S. Hou, W. Wang, and L. Wang. Numerical method for solving matrix coefficient elliptic equation with sharp-edged interfaces. *Journal of Computational Physics*, 229:7162–7179, 2010.
- [17] Y. Zhou, S. Zhao, M. Feig, and G. Wei. High order matched interface and boundary method for elliptic equations with discontinuous coefficients and singular sources. *Journal of Computational Physics*, 213:1–30, 2006.
- [18] S. Yua, Y. Zhou, and G. Wei. Matched interface and boundary (MIB) method for elliptic problems with sharp-edged interfaces. *Journal of Computational Physics*, 224:729–756, 2007.
- [19] Y. Zhou, J. Liu, and D. L. Harry. A matched interface and boundary method for solving multi-flow Navier–Stokes equations with applications to geodynamics. *Journal of Computational Physics*, 231:213–242, 2012.
- [20] Z.J. Cendes, D.N. Shenton, and H. Shahnasser. Magnetic field computation using Delaney triangulation and complementary finite element methods. *IEEE Trans. Magn.*, 19:2251–2554, 1983.
- [21] I. Babuska and S.A. Sauter. Is the pollution effect of the FEM avoidable for the Helmholtz equation considering high wave number? *SIAM Journal of Numerical Analysis*, 34:2392–2423, 1997.
- [22] S. Hou and X.-D. Liu. A numerical method for solving variable coefficient elliptic equation with interfaces. *Journal of Computational Physics*, 202:411–445, 2005.
- [23] Q. Shen. Local RBF-based differential quadrature collocation method for the boundary layer problems. *Engineering Analysis with Boundary Elements*, 34:213–228, 2010.
- [24] Siraj-ul-Islam and M. Ahmad. Meshless analysis of elliptic interface boundary value problems. *Engineering Analysis with Boundary Elements*, 92:38–49, 2017.

- [25] B. Martin and B. Fornberg. Seismic modeling with radial basis function-generated finite differences (RBF-FD) – a simplified treatment of interfaces. *Journal of Computational Physics*, 35:828–845, 2017.
- [26] B. Martin and B. Fornberg. Using radial basis function-generated finite differences (RBF-FD) to solve heat transfer equilibrium problems in domains with interfaces. *Engineering Analysis with Boundary Elements*, 79:38–48, 2017.
- [27] M. Ahmad and Siraj-ul-Islam. Meshless analysis of parabolic interface problems. *Engineering Analysis with Boundary Elements*, 94:134–152, 2018.
- [28] B. C. Shin and J. H. Jung. Spectral collocation and radial basis function methods for one-dimensional interface problems. *Applied Numerical Mathematics*, 61:911–928, 2011.
- [29] Siraj-ul-Islam, V. Singh, and S. Kumar. Estimation of dispersion in an open channel from an elevated source using an upwind local meshless method. *International Journal of Computational Methods*, 14(02):1750009, 2017.
- [30] Siraj-ul-Islam and V. Singh. A local meshless method for steady state convection dominated flows. *International Journal of Computational Methods*, 14(06):1750067, 2017.
- [31] V. Singh, Siraj-ul-Islam, and R. K. Mohanty. Local meshless method for convection dominated steady and unsteady partial differential equations. *Engineering with Computers*, 35:803–812, 2019.
- [32] R. Schaback. Error estimates and condition numbers for radial basis function interpolation. *Advances in Computational Mathematics*, 3:251–264, 1995.
- [33] Scott A. Sarra. Integrated multiquadric radial basis function approximation methods. *Computers & Mathematics with Applications*, 51(8):1283–1296, 2006.
- [34] Siraj-ul-Islam, I. Aziz, and M. Ahmad. Numerical solution of two-dimensional elliptic PDEs with nonlocal boundary conditions. *Computers and Mathematics with Applications*, 69:180–205, 2015.
- [35] S. Rippa. An algorithm for selecting a good value for the parameter c in radial basis function interpolation. *Advances in Computational Mathematics*, 11(2):193–210, 1999.
- [36] O. Davydov and D. T. Oanh. On the optimal shape parameter for Gaussian radial basis function finite difference approximation of the Poisson equation. *Computers and Mathematics with Applications*, 62:27–49, 2001.
- [37] C. S. Huang, H. D. Yen, and A. H. D. Cheng. On the increasingly flat radial basis function and optimal shape parameter for the solution of elliptic PDEs. *Engineering Analysis with Boundary Elements*, 34:802–809, 2010.
- [38] Michael Scheuerer. An alternative procedure for selecting a good value for the parameter c in RBF-interpolation. *Advances in Computational Mathematics*, 34(1):105–126, 2011.
- [39] M. Esmailbeigi and M. Hosseini. A new approach based on the genetic algorithm for finding a good shape parameter in solving partial differential equations by Kansa’s method. *Applied Mathematics and Computation*, 249:419–428, 2014.

- [40] S. Kazem and F. Hadinejad. Promethee technique to select the best radial basis functions for solving the two-dimensional heat equations based on hermite interpolation. *Engineering Analysis with Boundary Elements*, 50:29–38, 2015.
- [41] B. Fornberg and G. Wright. Stable computation of multiquadric interpolants for all values of the shape parameter. *Comput. Math. Appl.*, 48(5-6):853–867, 2004.
- [42] Bengt Fornberg and Cécile Piret. A stable algorithm for flat radial basis functions on a sphere. *SIAM J. Sci. Comput.*, 30(1):60–80, 2007/08.
- [43] Bengt Fornberg, Elisabeth Larsson, and Natasha Flyer. Stable computations with Gaussian radial basis functions. *SIAM J. Sci. Comput.*, 33(2):869–892, 2011.
- [44] Bengt Fornberg, Erik Lehto, and Collin Powell. Stable calculation of Gaussian-based RBF-FD stencils. *Comput. Math. Appl.*, 65(4):627–637, 2013.
- [45] Elisabeth Larsson, Erik Lehto, Alfa Heryudono, and Bengt Fornberg. Stable computation of differentiation matrices and scattered node stencils based on Gaussian radial basis functions. *SIAM J. Sci. Comput.*, 35(4):A2096–A2119, 2013.
- [46] P. K. Mishra, G. E. Fasshauer, M. K. Sen, and L. Ling. A stabilized radial basis-finite difference (RBF-FD) method with hybrid kernels. *Computers & Mathematics with Applications*, 77(9):2354–2368, 2019.
- [47] Bengt Fornberg and Natasha Flyer. Fast generation of 2-D node distributions for mesh-free PDE discretizations. *Comput. Math. Appl.*, 69(7):531–544, 2015.
- [48] G. E. Fasshauer and J. G. Zhang. On choosing of optimal shape parameters for RBF approximation. *Numerical Algorithms*, 45(1-4):345–368, 2007.
- [49] Shmuel Rippa. An algorithm for selecting a good value for the parameter c in radial basis function interpolation. *Advances in Computational Mathematics*, 11(2-3):193–210, 1999.
- [50] K. Xiaa, M. Zhanb, and G. W. Wei. MIB Galerkin method for elliptic interface problems. *Journal of Computational and Applied Mathematics*, 272:195–220, 2014.